

CORRECTION

Correction: Low-resolution vision in a velvet worm (Onychophora) (doi: 10.1242/jeb.175802)

John D. Kirwan, Josefine Graf, Jochen Smolka, Georg Mayer, Miriam J. Henze and Dan-Eric Nilsson

There was an error published in Journal of Experimental Biology (2018) **221**, jeb175802 (doi: 10.1242/jeb.175802).

In Materials and Methods, ‘Object taxis’, the final sentence should read: ‘An animal contributed only one trial to each experiment except for the two smaller bar targets, for which individuals were assessed up to four times.’

In addition, there were typing errors in the ‘Individual’ column (rows 89, 90 and 91) and ‘Target arc angle’ column (row 248) in Table S2; these values have been corrected.

None of the changes affects the conclusions of the paper. The authors apologise for any inconvenience this may have caused.

RESEARCH ARTICLE

Low-resolution vision in a velvet worm (Onychophora)

John D. Kirwan¹, Josefine Graf¹, Jochen Smolka¹, Georg Mayer², Miriam J. Henze^{1,3,*} and Dan-Eric Nilsson^{1,*}

ABSTRACT

Onychophorans, also known as velvet worms, possess a pair of simple lateral eyes, and are a key lineage with regard to the evolution of vision. They resemble ancient Cambrian forms, and are closely related to arthropods, which boast an unrivalled diversity of eye designs. Nonetheless, the visual capabilities of onychophorans have not been well explored. Here, we assessed the spatial resolution of the onychophoran *Euperipatoides rowelli* using behavioural experiments, three-dimensional reconstruction, anatomical and optical examinations, and modelling. Exploiting their spontaneous attraction towards dark objects, we found that *E. rowelli* can resolve stimuli that have the same average luminance as the background. Depending on the assumed contrast sensitivity of the animals, we estimate the spatial resolution to be in the range 15–40 deg. This results from an arrangement where the cornea and lens project the image largely behind the retina. The peculiar ellipsoid shape of the eye in combination with the asymmetric position and tilted orientation of the lens may improve spatial resolution in the forward direction. Nonetheless, the unordered network of interdigitating photoreceptors, which fills the whole eye chamber, precludes high-acuity vision. Our findings suggest that adult specimens of *E. rowelli* cannot spot or visually identify prey or conspecifics beyond a few centimetres from the eye, but the coarse spatial resolution that the animals exhibited in our experiments is likely to be sufficient to find shelter and suitable microhabitats from further away. To our knowledge, this is the first evidence of resolving vision in an onychophoran.

KEY WORDS: Eye, Vision, Spatial resolution, Object taxis, Visually guided behaviour, *Euperipatoides rowelli*

INTRODUCTION

Onychophora (velvet worms) represent a crucial taxon for understanding the evolution of vision. Onychophorans and tardigrades (water bears) are the closest living relatives of arthropods (chelicerates, myriapods, crustaceans and hexapods) (Giribet, 2016), which account for the majority of described animal species on Earth (Zhang, 2011, 2013) and boast an unrivalled diversity of visual systems and visual ecology (Land and Nilsson, 2012). To understand the origin and evolution of the sophisticated eyes of arthropods, it is essential to investigate their closest outgroups.

Onychophorans and tardigrades possess a pair of simple lateral eyes (Greven, 2007; Mayer, 2006; Martin et al., 2017). However,

tardigrades are microscopic animals (Gross et al., 2015), which makes it challenging to study their behaviour. Furthermore, they display many characteristics that are possibly derived because of miniaturization (Dewel and Dewel, 1998; Schmidt-Rhaesa, 2001). To date, the homology of their eyes with the visual systems of arthropods has not been resolved. Tardigrade eyes might be innovations specific to their own lineage (Greven, 2007; Martin et al., 2017), although an orthologue of the visual r-opsins (rhabdomeric opsins) of arthropods has been identified in the tardigrade *Hypsibius dujardini* (Hering and Mayer, 2014). In contrast, onychophorans are predators of one to several centimetres in length, inhabiting humid, terrestrial environments (Mayer et al., 2015). Several aspects of their anatomy are strikingly similar to that of Cambrian lobopodians (Smith and Caron, 2015; Smith and Ortega-Hernández, 2014), an assemblage of marine animals with cylindrical bodies and clawed feet, which probably includes the ancestors of extant panarthropods (onychophorans, tardigrades and arthropods) (Liu and Dunlop, 2014). The eyes of onychophorans exhibit a potentially ancestral design, and it has been proposed that they are homologous to arthropod eyes (Mayer, 2006; Strausfeld et al., 2006). A single r-opsin, named onychopsin (Hering et al., 2012), is expressed in the photoreceptors of the retina (Beckmann et al., 2015). Visual r-opsins of arthropods are orthologues of onychopsin, having diverged after the Arthropoda–Onychophora split (Henze and Oakley, 2015; Hering et al., 2012), which supports the underlying homology of vision in the two clades. Interestingly, the onychophoran eye is most sensitive to blue light of about 480 nm (Beckmann et al., 2015), similar to many monochromatic marine animals (Marshall et al., 2015), and this may be an ancestral feature.

On account of their phylogenetic position, resemblance to fossil lobopodians, structural and genetic homologies to arthropods, and size, onychophorans are a key clade for understanding the function of the eyes in the last common ancestor of panarthropods. Ultimately, it is selective pressure on the performance of visual tasks that drives the evolution of visual systems (Nilsson, 2013), and functional investigations are a necessary component of understanding why a system occurs and has evolved (Nilsson, 1994; Nilsson et al., 2005; Petie et al., 2016). However, despite their importance, the visual capabilities of onychophorans have not been well explored.

Here, we investigated the spatial resolution of *Euperipatoides rowelli*, a nocturnal, forest-dwelling species native to eastern Australia (Oliveira et al., 2012), which has been at the forefront of evolutionary and developmental studies on Onychophora (e.g. Blaxter and Sunnucks, 2011; Franke et al., 2015; Mayer et al., 2015). Spatial resolution is defined as the angular distance between two points that are just distinguishable by the visual system. It is conventionally given as the period of a sine wave, with each of the points representing a maximum, while the sampling resolution (inter-receptor angle) must be half the period of the sine wave, allowing neighbouring receptors to sample a maximum (bright point) and a minimum (dark space between the points). Optical resolution is the limit imposed by the blurring of the optics, which is often simulated as a Gaussian function. In an optimized visual

¹Lund Vision Group, Department of Biology, Lund University, 223 62 Lund, Sweden.

²Department of Zoology, University of Kassel, 34132 Kassel, Germany.

³Queensland Brain Institute, University of Queensland, St Lucia 4072, QLD, Australia.

*These authors share senior authorship.

†Authors for correspondence (dan-e.nilsson@biol.lu.se, miri@mhenze.net)

© J.D.K., 0000-0001-5537-3574; J.G., 0000-0002-7380-470X; J.S., 0000-0003-2958-0697; G.M., 0000-0003-0737-2440; M.J.H., 0000-0002-0563-2539; D.-E.N., 0000-0003-1028-9314

system, the blurring induced by the optics matches the spatial resolution that the photoreceptors provide, such that excellent optics are not wasted on an under-sampling retina and an over-sampling retina is not wasted on poor optics. To examine the image-forming capacity of the eyes of *E. rowelli*, we developed a geometrical model based on a three-dimensional (3D) reconstruction, and anatomical and optical measurements. In a behavioural assay, we tested whether the animals headed for a dark target, ostensibly representing shelter, in a pattern of different widths, which was on average isoluminant with the background. The two stimulus patterns closest to the behavioural detection threshold were then used to estimate the spatial resolution of *E. rowelli* by simulating the blurring effect of the eye's optics in a theoretical model.

MATERIALS AND METHODS

Animals

Specimens of *Euperipatoides rowelli* Reid (1996), were collected from decomposing logs in the Tallaganda State Forest (35°26'S, 149°33'E, 954 m) under permit no. SL100159 from the Forestry Commission of New South Wales, Australia. Adults and their offspring were kept individually in plastic containers with perforated lids at 19°C under a light:dark cycle of 12 h:12 h. The containers comprised a layer of peat covered with damp paper tissues, which were moistened weekly. We fed small (≤ 10 mm) crickets to the onychophorans every 3 weeks, and replaced peat and tissues 1 or 2 days afterwards.

Light response

To exclude potentially blind animals from further experiments, we tested whether they avoided bright light, a spontaneous response that has previously been demonstrated in *E. rowelli* (Beckmann et al., 2015). Each individual was dark-adapted for 3 min, after which broad-spectrum light from a xenon arc lamp (450 W, Malipiero AV

Technik, Zurich, Switzerland) was directed through a UV–VIS-transmitting light guide at the animal's head from a distance of 7 cm (intensity $>10^{14}$ photons $\text{cm}^{-2} \text{s}^{-1}$). Animals that did not respond to the light beam by retracting the head, a change of direction or an increase in speed in any of five trials were excluded from the study. This was the case for one of 52 individuals. One of the remaining animals was directly killed for 3D reconstruction of its head and eyes, while the other 50 were subjected to behavioural experiments before they were randomly chosen for anatomical or optical investigations.

Anatomy

For anatomical measurements and examination (Table 1, Figs 1 and 2), three light-adapted specimens of 32–40 mm body length were anaesthetized using CO_2 . Their heads were severed between the slime papillae and the first or second pair of legs, fixed in 2% or 2.5% glutaraldehyde and 2% paraformaldehyde in 0.1 mol l^{-1} sodium cacodylate buffer (pH 7.1 or 7.4) at 4°C for 12 h, and washed repeatedly in buffer. Two heads used for both light and electron microscopy were post-fixed in 1% osmium tetroxide in buffer for 2 h and washed again. All three samples were then dehydrated in an ethanol series, rinsed with acetone, pre-embedded in Epon for over 12 h, and embedded in fresh Epon, which was polymerized for 48 h at 60°C.

The two osmium-treated heads were halved along the sagittal plane, trimmed and oriented in an RMX PTX microtome (Boeckeler Instruments Inc., Tucson, AZ, USA) such that the eyes were cut through their centre at different angles. Sections of 3 μm thickness were mounted on glass slides, stained with 1% Toluidine Blue in 1% borax and photographed under a Zeiss Axiophot light microscope (Jena, Germany) with a Nikon DS-Fi2-U3 CCD camera (Tokyo, Japan). Ultrathin sections were mounted on copper grids, stained with 2% uranyl acetate and lead citrate in distilled water, and studied with a JEOL 1230 transmission electron microscope (Tokyo, Japan).

Table 1. Properties of the eyes of *Euperipatoides rowelli* determined in this study

Structure	Property	Source	<i>n</i>	<i>e</i>	<i>i</i>	Mean (μm)	s.d. (μm)
Lens	Radius of curvature of front surface ($R_{1,\text{lens}}$)	Isolated fresh lenses	6	6	4	56.1	1.7
		LM sections	15	2	1	58.1	1.0
	Radius of curvature of rear surface ($R_{2,\text{lens}}$)	Isolated fresh lenses	6	6	4	−54.8	2.0
		Isolated fresh lenses	6	6	4	104.5	4.1
	Axial thickness (d_{lens})*	LM sections	18	5	3	63.6	7.9
		EM sections	2	2	2	64.2	1.4
		3D reconstruction	4	2	1	72.6	
		Isolated fresh lenses	10	10	6	105.0	2.8
	Equatorial diameter (widest diameter)	LM sections	19	5	3	79.0	19.7
		EM sections	2	2	2	76.4	9.4
		3D reconstruction	4	2	1	96.8	
Cornea	Distance between equator and back vertex of the lens	Isolated fresh lenses	6	6	4	54.4	6.8
		Isolated fresh lenses	10	10	6	275.0	11.6
	Measured focal length (f_{lens}) in saline					272.0	
	Corrected focal length (f_{lens}) in saline						
	Radius of curvature (R_{cornea})	LM sections	5	3	2	55.0	1.0
		LM sections	18	5	3	12.2	3.3
	Thickness (d_{cornea})*	EM sections	2	2	2	11.0	2.3
		3D reconstruction	4	2	1	8.7	
	Retina	LM sections	18	5	3	49.9	12.9
		EM sections	2	2	2	40.1	13.3
		3D reconstruction	4	2	1	52.0	
Eye	Distance between principal point (P_{eye}) and back vertex of the lens	Eqn 6				−25.0	
		Eqn 4				156.4	
	Back focal distance (focal distance given from the back vertex of the lens)					131.4	

The most accurate estimate of the refractive index of the lens was 1.485. *Measurements taken along the shortest axis (axis of symmetry) through the centre of the lens; LM, light microscopic; EM, electron microscopic; *n*, number of measurements; *e*, number of eyes; *i*, number of individuals. Measurements were first averaged for each eye, then for each individual, and finally for all individuals. The standard deviation (s.d.) gives individual differences. Body lengths of the measured specimens varied from 27 to 40 mm.

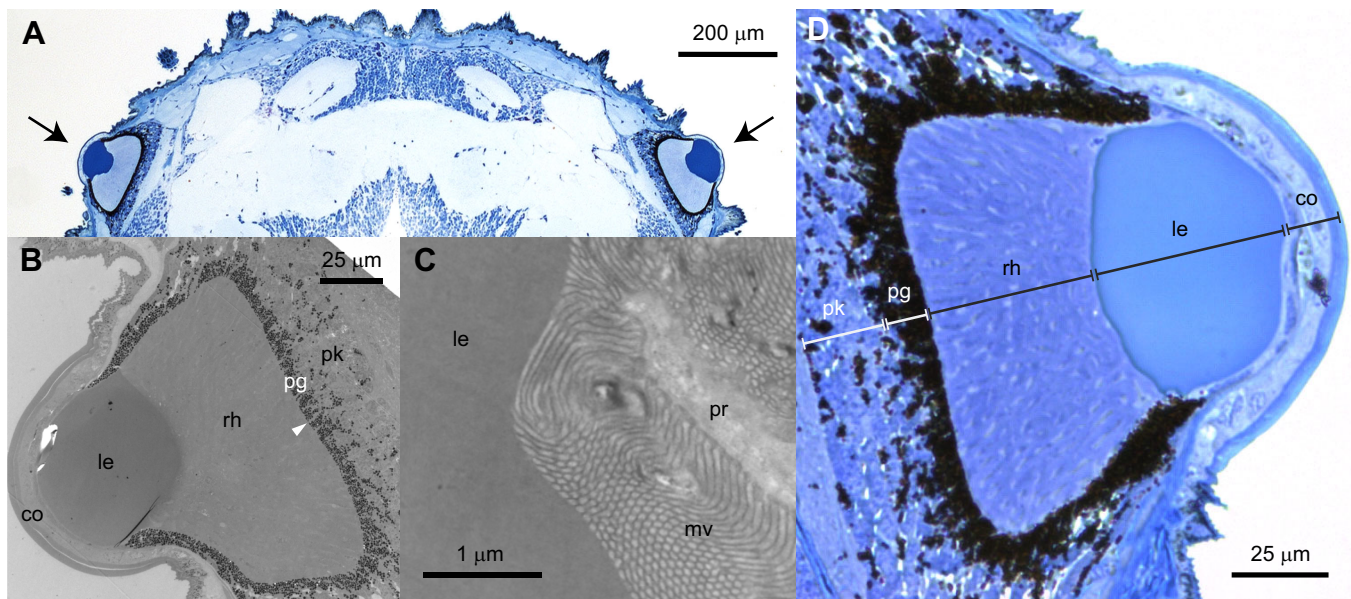


Fig. 1. Anatomical characteristics of the eyes of *Euperipatoides rowelli*. (A) Section through the dorsal part of the head, stained with Toluidine Blue. Dorsal is up. The eyes (arrows) are located dorsolaterally on each side of the head. (B) Transmission electron micrograph of a section through the eye. Distal is to the left. The cornea (co) consists of several layers, of which the outermost is the old cuticle to be shed. The underlying lens (le) appears homogeneous. Directly proximal to the lens follows the light-sensitive rhabdomeric layer (rh), surrounded by dark screening pigment (pg). The nuclei of photoreceptors and pigment cells are located in the perikaryal layer (pk) below the pigment layer. Photoreceptor processes connect the distal and proximal parts of the photoreceptor cell. The arrowhead points at a position where such a process penetrates the pigment layer. (C) Higher magnification of the transition from the lens to the rhabdomeric layer in an electron micrograph. Curved microvilli (mv) branch off from photoreceptor processes (pr) in different directions. Some of them are in direct contact with the rear surface of the lens (le). (D) Section through the eye, stained with Toluidine Blue. Distal is to the right. There are no gaps between the cornea (co) and the lens (le), or between the lens and the rhabdomeric layer (rh). A disorganized pattern of processes and microvilli is discernible in the retina.

The third head was used to make a complete series of 3 µm transverse light-microscopic sections from the antennal roots to the slime papillae. We processed and imaged the sections as described above and aligned them in Amira 5.3.3 (FEI Visualization Sciences Group, Burlington, MA, USA) for 3D reconstruction (Fig. 2; Movie 1). The structures of the eyes were reconstructed from 250× image stacks and integrated into the head, which was retraced from 50× image stacks. An anteroposterior section through the centre of the lens of the left eye in the 3D reconstruction served as a template for the geometrical model of the eye (Fig. 4) created in Adobe Illustrator CS6 (16.0.2, Adobe Systems Inc., San Jose, CA, USA).

Optical examinations, measurements and calculations

To check for major gradients in refractive index of the lens, one adult specimen was anaesthetized with chloroform and decapitated. The head was embedded in freezing medium in a plastic mould (Tissue-Tek O.C.T. Compound and Tissue-Tek Cryomold, Sakura Finetek Europe B.V., Alphen aan den Rijn, The Netherlands) and immediately frozen in ethanol cooled by dry ice. Sections of 10–12 µm thickness were cut at –20°C on a cryostat (CM3050 S, Leica Biosystems, Nussloch, Germany), mounted on SuperFrost Plus slides (Menzel-Gläser, Braunschweig, Germany) and stored at –80°C. Directly before examination, the sections were defrosted and lightly fixed in 4% paraformaldehyde in distilled water for 10 min, washed in distilled water, and embedded in ProLong Gold Antifade Mountant (Thermo Fisher Scientific, Waltham, MA, USA). Differential interference contrast (DIC) images of the eyes (Fig. S1) were taken under a Zeiss Axio Imager M2 microscope with a Zeiss Axiocam 503 colour camera using the software ZEN 2 (Carl Zeiss AG, Oberkochen, Germany).

When we dissected the eyes of specimens of *E. rowelli* to isolate the optical components, the lens invariably detached from the cornea. Therefore, we determined the focal length of the entire eye in several steps by measuring the focal length of the isolated lens in saline, assessing its dimensions, calculating its refractive index, and estimating the focal length of the combination of cornea and lens in an intact eye. The whole procedure is detailed below.

Specimens of 27–39 mm body length were anaesthetized with CO₂. Their head was severed, placed in a saline solution based on the ion concentrations of onychophoran haemolymph (Robson et al., 1966), and opened along the sagittal plane. An incision into the eye cup was sufficient to isolate the lens, which simply popped out. We measured the focal length of 10 fresh lenses from six individuals under a bright-field microscope (Labophot-2, SN 440152, Nikon Corporation, Tokyo, Japan) using a 20× objective. Each lens was immersed in saline between a microscope slide and a coverslip held apart by a spacer of about 1 mm, and positioned such that the axial path of light through the lens corresponded to that of the intact onychophoran eye. The condenser of the microscope was removed and a grid of dark stripes on translucent plastic film was placed atop the open field diaphragm. Compared with the size of the lens, this object was at infinity, such that incident rays were parallel and the image plane coincided with the back focal plane. The equator of the lens was then brought into focus (Fig. 3B), and the stage was gradually raised until the image of the grid pattern produced by the onychophoran lens was in focus (Fig. 3C). The necessary change in position of the stage, which was given by a micrometre gauge, was taken as a first approximation of the focal length of the lens in saline (f'_{lens}).

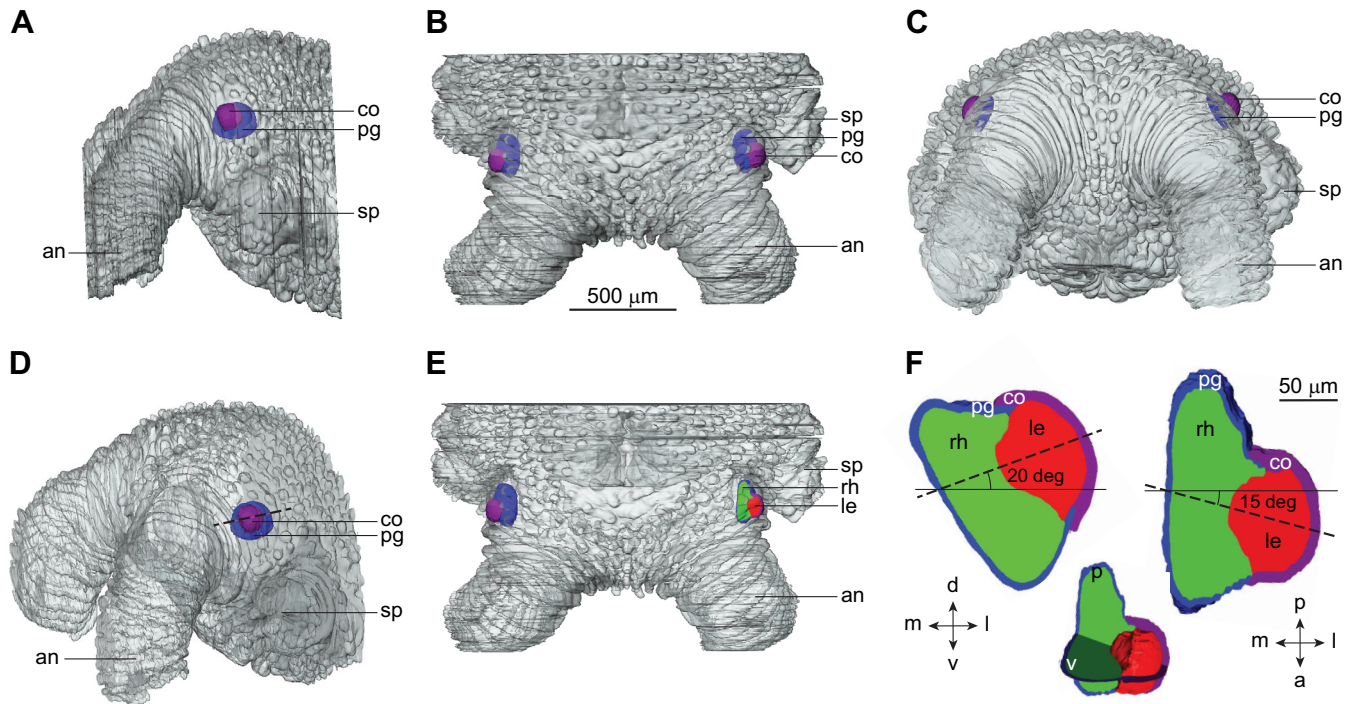


Fig. 2. Three-dimensional (3D) reconstruction of the head and eyes of *E. rowelli*. The surface of the head is shown partially transparent to expose the internal eye structures. (A) Lateral, (B) dorsal and (C) frontal view of the 3D reconstruction. The eyes are positioned on either side of the head right behind the antennae and point slightly upwards. (D) Slanted view of the head with a dashed line indicating the plane of the section through the left eye shown in E. (E) Dorsal view of the head showing an anteroposterior section through the centre of the lens of the left eye. (F) Dorsoventral (left) and anteroposterior (right) section through the centre of the lens of the left eye, as indicated by the small figure in the centre (not to scale). The dashed line marks the intersection of the two sectional planes and coincides with the shortest axis through the centre of the lens. This axis deviates by about 20 deg upward and 15 deg frontward from a mediolateral orientation (continuous line). Directions: a, anterior; d, dorsal; l, lateral; m, medial; p, posterior; v, ventral. Anatomical structures: an, antennae; co, cornea; le, lens; pg, pigment layer; rh, rhabdomic layer; sp, slime papilla. The scale bar in B applies to A–E. Body length of animal when alive, 32 mm.

To determine the radii of curvature of the front and rear surfaces of the lens, its axial thickness (thickness along the symmetry axis) and the distance between the equator and back vertex, the lens was oriented such that its axis of symmetry was horizontal (Fig. 3A). Images of six lenses from four individuals were taken from directly above with a Nikon D5100 digital camera (Nikon Corporation) through the 20× objective of the microscope.

The approximate refractive index of the lens n'_{lens} was then calculated using the lensmaker's equation for thick lenses (Hecht and Zajac, 1974):

$$\frac{1}{f'_{\text{lens}}} = \frac{n'_{\text{lens}} - n_{\text{saline}}}{n_{\text{saline}}} \times \left[\frac{1}{R_{1,\text{lens}}} - \frac{1}{R_{2,\text{lens}}} + \frac{(n'_{\text{lens}} - n_{\text{saline}}) \times d_{\text{lens}}}{n'_{\text{lens}} \times R_{1,\text{lens}} \times R_{2,\text{lens}}} \right], \quad (1)$$

where f'_{lens} is the focal length of the lens in saline determined as described above, $n_{\text{saline}}=1.3345$ is the refractive index of the surrounding saline, measured with a refractometer (Jena 211561, Preisler, Malmö, Sweden), $R_{1,\text{lens}}$ and $R_{2,\text{lens}}$ are the radius of curvature of the front and rear surface of the lens, respectively, and d_{lens} is the axial thickness of the lens.

To revise this approximation, we determined the position of the second principal point of the lens P_{lens} , from which the focal length is conventionally measured, as follows:

$$P_{\text{lens}} = \frac{n'_{\text{lens}} \times d_{\text{lens}}}{k_{\text{lens}}} \times \frac{n'_{\text{lens}} - n_{\text{saline}}}{n'_{\text{lens}} \times R_{1,\text{lens}}}, \quad (2)$$

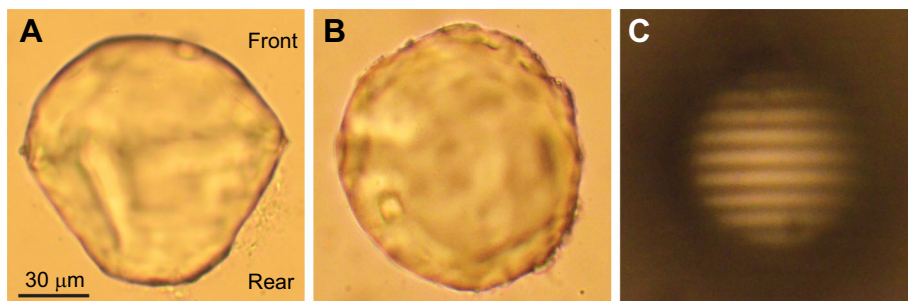


Fig. 3. The isolated lens of the eye of *E. rowelli* can produce images of distant objects. (A) Fresh lens of an animal of 3 cm body length in lateral view. The lens has a curved front surface, which is adjacent to the cornea in an intact eye. Its diameter tapers conically towards the curved rear. (B) Same lens in rear view, with the camera focused on the lens equator (widest diameter). (C) Image of a grid pattern (dark stripes on translucent paper) produced above (behind) the equator by the lens in B. The scale bar in A applies to all three panels.

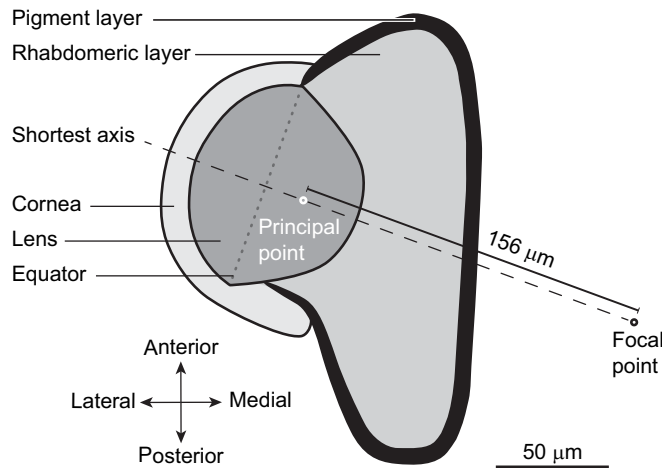


Fig. 4. Geometrical model of the eye of *E. rowelli*. Anatomical dimensions are based on the anteroposterior section through the 3D reconstruction of the left eye shown in Fig. 2. To conform to conventional eye models, the representation has been rotated. Data for the combined optical system of the cornea and lens rely on measurements and equations given in Materials and Methods and in Table 1. The dashed black line indicates the shortest axis through the centre of the idealized lens, which is also the axis of symmetry. Circles give estimates of the position of the principal and focal point along this axis. A focal length of approximately 156 μm from the principal point places the focal point well behind the rhabdomeric layer in the central part of the eye.

where k_{lens} is:

$$k_{\text{lens}} = \frac{n'_{\text{lens}} - n_{\text{saline}}}{R_{1,\text{lens}}} + \frac{n_{\text{saline}} - n'_{\text{lens}}}{R_{2,\text{lens}}} - d_{\text{lens}} \times (n'_{\text{lens}} - n_{\text{saline}}) \times \frac{n_{\text{saline}} - n'_{\text{lens}}}{n'_{\text{lens}} \times R_{1,\text{lens}} \times R_{2,\text{lens}}}. \quad (3)$$

A more accurate estimate of the focal length of the lens was obtained by subtracting the distance between the equator and the back vertex from the first estimate of the focal length, and by incorporating the distance between the back vertex and the second principal point instead. The corrected value of f_{lens} was used to recalculate the refractive index of the lens n_{lens} , applying Eqn 1.

As the cornea of *E. rowelli* is perfectly flush with the adjacent lens (Fig. 1), thin compared with the lens, and with a radius of curvature R_{cornea} in the same range as that of the lens front (Table 1), it was subsumed into the lens assuming the same refractive index. The focal length of the eye f_{eye} could thus be calculated for the combined thickness d of the lens and cornea with air ($n_{\text{air}}=1.0003$) in front of the cornea and rhabdomeres ($n_{\text{rhabdomere}}=1.363$; Nilsson and Howard, 1989) behind the lens, using the following formula:

$$f_{\text{eye}} = \frac{n_{\text{lens}}}{k_{\text{eye}}}, \quad (4)$$

where k_{eye} is:

$$k_{\text{eye}} = \frac{n_{\text{lens}} - n_{\text{air}}}{R_{\text{cornea}}} + \frac{n_{\text{rhabdomere}} - n_{\text{lens}}}{R_{2,\text{lens}}} - d \times (n_{\text{lens}} - n_{\text{air}}) \times \frac{n_{\text{rhabdomere}} - n_{\text{lens}}}{n_{\text{lens}} \times R_{\text{cornea}} \times R_{2,\text{lens}}}. \quad (5)$$

The position of the second principal point P_{eye} of the combined optical system consisting of the cornea and lens in the intact eye was found as follows:

$$P_{\text{eye}} = \frac{n_{\text{rhabdomere}} \times d}{k_{\text{eye}}} \times \frac{n_{\text{lens}} - n_{\text{rhabdomere}}}{n_{\text{lens}} \times R_{\text{cornea}}}. \quad (6)$$

We determined the focal point of the eye on the shortest axis through the centre of the lens (symmetry axis) by adding the focal distance to the position of the second principal point of the eye, and integrated the results in a geometrical model (Fig. 4).

Object taxis

In a behavioural assay, we exploited object taxis to test the spatial resolution of *E. rowelli*. The setup consisted of a cylindrical arena with a diameter of 45 cm and a height of 36 cm (Fig. 5A). It was covered with a milk glass diffuser placed on top of the walls, and illuminated by a 100 W light bulb (Osram Sylvania, Danvers, MA, USA) mounted above the centre of the arena with a distance of 21 cm to the diffuser in an otherwise dark room. Taking the spectral sensitivity of *E. rowelli* into account (Beckmann et al., 2015), this light bulb was selected as the brightest of three artificial light sources, all of them with relative values in the same order of magnitude as the natural illumination at ground level in a copse on an overcast day (Fig. S2). To estimate the absolute amount of light perceivable by the onychophorans between 350 and 700 nm, we measured the direct radiance spectrum reaching the centre of the arena floor through the diffuser with a calibrated spectroradiometer (RSP900-R; International Light, Peabody, MA, USA). This curve was multiplied by the spectral sensitivity of *E. rowelli* (Beckmann et al., 2015) to account for the probability of absorption by the visual pigment, which resulted in an effective intensity of 1.79×10^{14} photons $\text{cm}^{-2} \text{s}^{-1}$.

In control experiments, the inner walls of the arena were lined with grey matte paper of a luminance of 45.2 cd m^{-2} , as determined from the centre of the arena by a ScreenMaster photometer (Hagner, Solna, Sweden). In tests, we presented either of two kinds of stimuli printed on matte paper on top of the grey background. Dual bar (Haar wavelet) stimuli comprised a black bar and an adjacent white bar of equal width (Fig. 5D,F). Piecewise sine stimuli consisted of a dark (negative) half-period sine flanked on each side by a light (positive) half-period sine of half the amplitude (Fig. 5E,G). While both types of stimuli are isoluminant against the grey background if averaged across their whole width, a prerequisite for our experiments, the piecewise sine stimulus was chosen because it is composed of fewer spatial frequencies than discrete bars. This reduces the risk that the animals use frequencies lower than the main spatial frequency of the stimulus to orient. The black part of the dual bars and the full width at half-minimum of the dark region in the piecewise sine are hereafter referred to as the target of the stimulus (Fig. 5D–G). Target sizes are given as angular width on the arena circumference. The widths of the dark targets in the dual bar stimuli were 12.7, 25.5 and 51 deg, and those of the piecewise sine stimuli were 2.2, 3.3, 4.4, 5.6, 6.7, 10, 13, 20, 27, 33 and 40 deg.

The floor of the arena was covered with laminated white matte paper fixed on a glass pane. Its centre was marked by crosshairs, visible only from below (Fig. 5B). For each trial, a single individual was transferred into the arena under a small lid on a piece of plastic, and released in the centre. The silhouette of the walking animal was recorded by a Sony camera (HDR-CX11E or HDR-CX730; Sony Corporation, Tokyo, Japan) from 73 cm below. A trial concluded when the animal made contact with the wall of the arena, or after

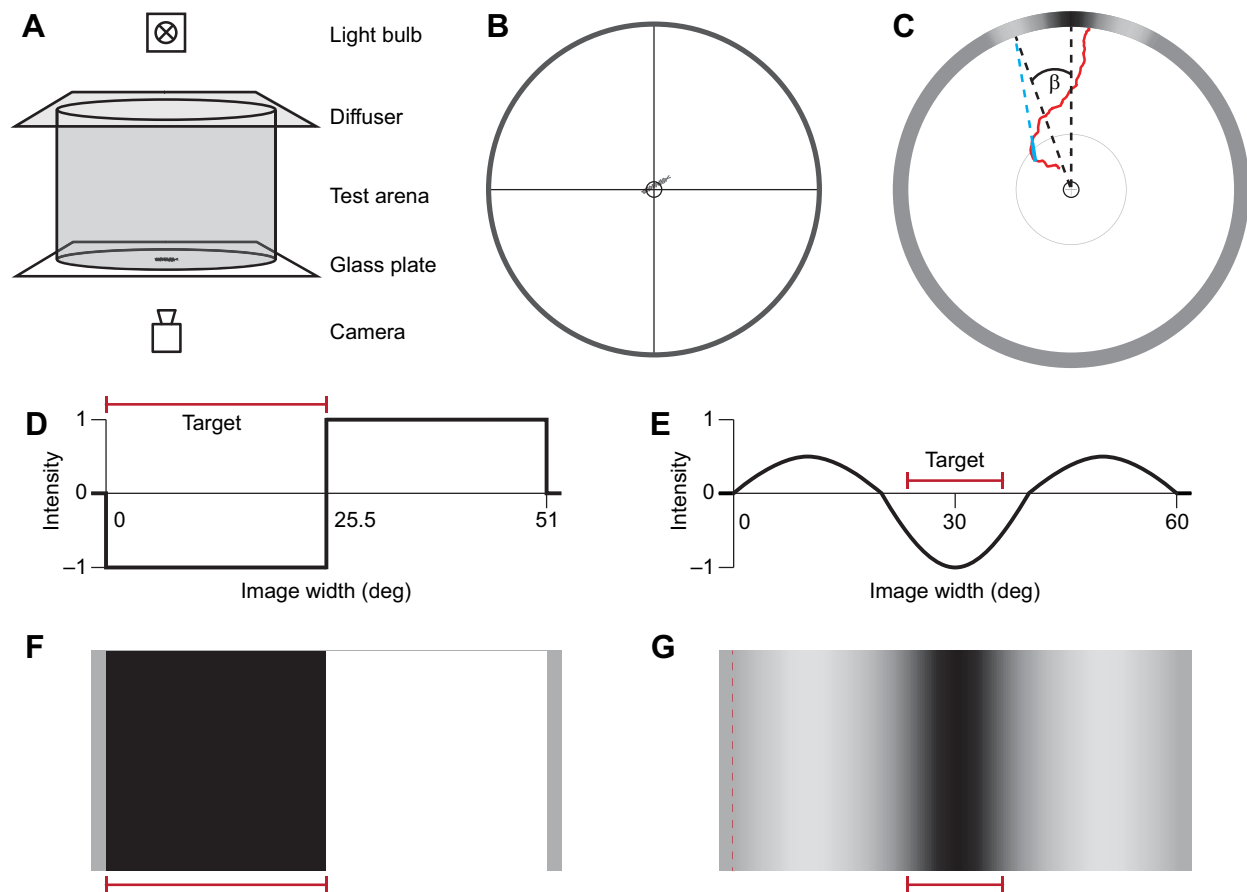


Fig. 5. Experimental setup. (A) Circular arena with light source (100 W light bulb) above and camera beneath. (B) The arena floor viewed from below with crosshairs as a reference and the silhouette of the animal visible through the paper lining of the bottom. (C) Diagram of how the heading (β) of the animal was determined based on its walking path from the centre to the arena wall. (D,E) Intensity profiles of two stimuli (F,G) used in the experiments. The x-axis denotes the angular position across the stimulus, while the y-axis gives the relative reflectance, with positive values being brighter and negative values being darker than medium-grey. A dual bar (Haar wavelet) stimulus comprises adjacent black and white bars of equal arc width (D,F), and the entire black bar forms the target (indicated by a continuous red line). In a piecewise sine stimulus (E,G), a dark (negative) half-period sine is flanked on each side by a bright (positive) half-period sine of half the amplitude. The target corresponds to the full width at half-minimum of the dark centre of the stimulus.

15 min. Between trials, the arena floor was cleaned and the setup was rotated 90 deg to control for other directional cues, such as chemical trails left by individuals in previous trials, the magnetic field of the Earth and the position of the experimenter. We tested specimens of 22–41 mm body length during the night phase of their circadian entrainment. An animal contributed only one trial to each experiment except for the two smaller bar targets, for which individuals were assessed up to three times.

Tracking and data analyses

We applied the Camera Calibration Toolbox (http://www.vision.caltech.edu/bouguetj/calib_doc/) for MATLAB (R2012b, MathWorks, Inc., Natick, MA, USA) to correct for distortions in the video recordings. The centre of the animal's head was marked frame by frame using Tracker 4.05 (<https://physlets.org/tracker/>), thus tracing the animal's walking path (Figs 5C and 6). To quantify the orientation towards the target, we determined the heading of the animal when it crossed a circle of 7.5 cm radius around the centre of the arena as it moved towards the wall (Fig. 5C). A line through the position of the animal's head 1 cm before and 1 cm after it crossed the circle defined the projected point of arrival (intersection of the line with the arena wall). The heading of the animal was calculated as the angular difference between the projected point of arrival and

the centre of the target, as seen from the arena centre. In controls, a random position on the background was chosen once, and then employed as the centre of an imaginary target in all trials.

We investigated whether there were unexpected clusters of headings in the control using Watson's test for a circular uniform distribution. The non-parametric Kruskal–Wallis rank sum test (Kruskal and Wallis, 1952) was applied to test for differences in the concentration of headings among all experiments of the same stimulus type, while Wilcoxon–Mann–Whitney tests were employed to compare specific sets of experiments.

Both the Kruskal–Wallis and the Wilcoxon–Mann–Whitney test assume independent samples, but we reused animals in the experiments. To account for our more complex data structure and to analyse additional effects, a different approach was taken. The proportion of animals heading towards the quadrant centred on the (imaginary) target (Fig. 7) was defined as the success rate (Fig. 8) and the headings were converted into binary data (success or failure). We then fitted a mixed-effects probit regression model to the data using the lme4 package (Bates et al., 2015) in R 3.4.1 (<https://www.R-project.org/>). This model is an implementation of the psychometric function of the response. A base rate of 25% was introduced using the psyphy package (<https://cran.r-project.org/package=psyphy>), given that this is the probability that the animal is

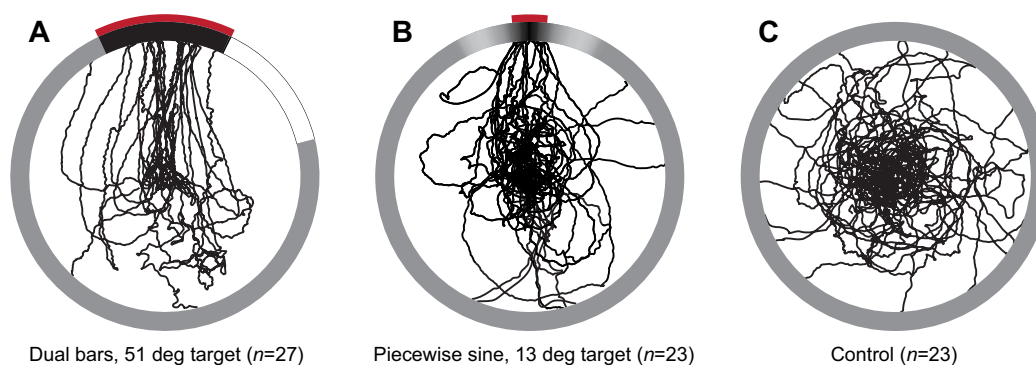


Fig. 6. Reconstructed walking paths of specimens of *E. rowelli* released individually in the centre of an arena of 45 cm diameter with different visual displays on the arena wall. (A) Dual bar stimulus of 51 deg target width. (B) Piecewise sine stimulus of 13 deg target width. (C) Featureless, medium-grey wall (control). The setup was cleaned and rotated 90 deg between trials. For illustration, all tracks have been normalized relative to the centre of the target in tests trials and are superimposed. The red arc indicates the target region and n is the number of individuals that contributed to the respective experiment.

heading to the target quadrant by chance. Two fixed effects on the success rate were considered: the size of the stimulus (target arc width) and the orientation of the target within the experimental room. The intercept of the fitted curve was allowed to vary to account for differences in responses between animals. We tested a set of predefined models (Table S1) and selected the most likely one based on the smallest value for the Akaike information criterion (AIC). The model was only fitted to trials with a piecewise sine target of 20 deg or smaller and the control. Bar targets were excluded, because their sizes are not directly comparable to those of

piecewise sine targets. Piecewise sine targets wider than 20 deg were also not analysed; their stimulus pattern exceeds 90 deg and is thus not entirely covered by the quadrant centred on the target, which changes the conditions for the binary division of the data we made. Regardless, these wide targets are not crucial for our study, as they are clearly above the detection threshold. To assess whether the probit regression model was correctly specified, we investigated the residuals in a diagnostic probability plot (Fig. S3) applying the R-package DHARMA (<https://CRAN.R-project.org/package=DHARMA>).

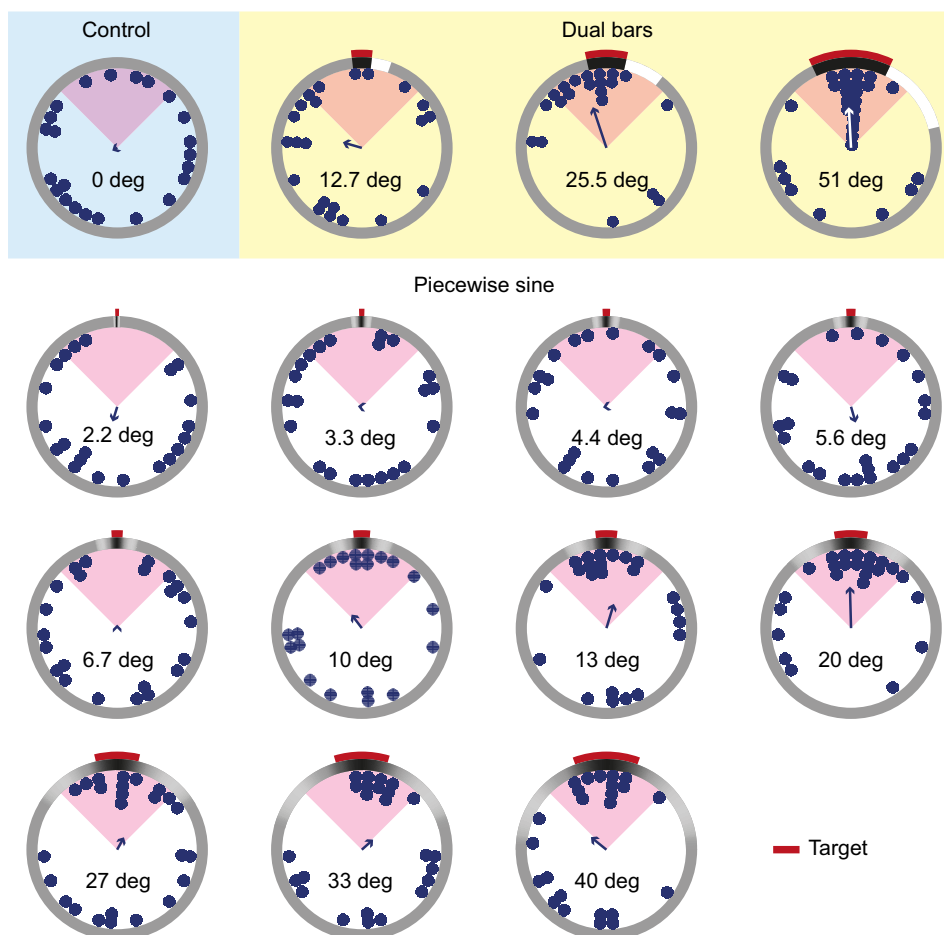


Fig. 7. Headings taken by specimens of *E. rowelli* from the centre of the arena towards visual displays on the arena wall. For details, see Fig. 5C. Upper left (blue shading), control experiment with a medium-grey background. Upper right (yellow shading), experiments with dual bars. Lower three rows (no shading), a pattern of piecewise sines. The ring indicates the visual display on the arena wall, and the red arc the dark target region. Headings (dark-blue dots) are binned by 5 deg increments. Arrows give the resultant vector of all headings. The quadrant counted as the correct direction towards the target to calculate the success rate in Fig. 8 is shaded light red. In the control, this quadrant was chosen randomly.

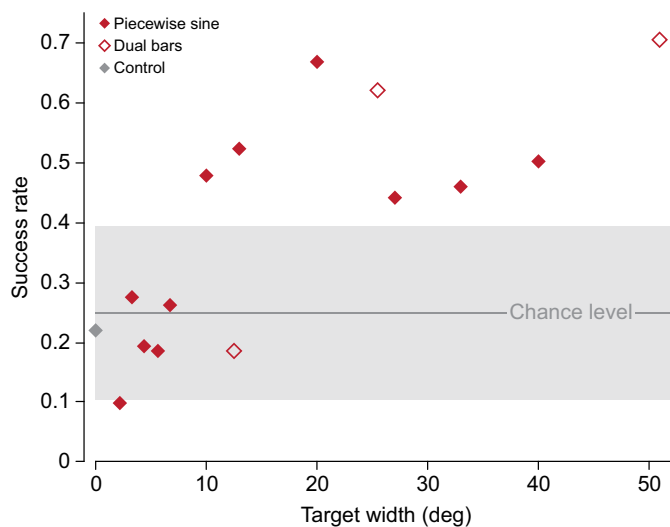


Fig. 8. Success rate in the experiments on object taxis plotted against the width of the target. The success rate was calculated as the proportion of individuals heading towards the target quadrant defined in Fig. 7. On average, we expect 0.25 of the headings in each quarter of the circle, if the onychophorans cannot detect the target. To estimate the expected variation, the imaginary target quarter in the control was rotated by 360 deg in increments of 1 deg. The shaded grey area marks the maximal deviation of the resulting 'success' rate above and below the chance level, i.e. these values can result from a statistically homogeneous distribution without any target. Note that the target sizes of the dual bar and the piecewise sine stimuli are not directly comparable.

Estimating spatial resolution

We estimated the spatial resolution of *E. rowelli* from the behaviourally determined detection threshold, assuming a plausible range of contrast sensitivities. The reason for this approach was that all our stimuli comprised more than one spatial frequency, which did not allow us to directly infer spatial resolution from behavioural responses. Instead, we calculated optical resolution by determining how the just-detectable piecewise sine stimulus and the next smaller pattern appeared through the optics of the under-focused onychophoran eye. In a theoretical model implemented in MATLAB (R2012b, MathWorks, Inc.), a perfect image of the respective piecewise sine pattern was blurred with a Gaussian filter until the percentage of Michelson contrast between the dark minimum and bright maxima of the stimulus dropped to a threshold value (Fig. 9). This threshold is the minimal contrast that still allows the animal to resolve the pattern in the blurred image. It depends on the animal's contrast sensitivity and is its reciprocal value in per cent. As contrast sensitivities of onychophorans are unknown, we determined the optical resolution for 10 potential threshold contrasts between 5% and 20% based on measurements from other species (see Discussion for references). Intermediate values were interpolated using a smoothing spline in R 3.4.1 (<https://www.R-project.org>). The full width at half-maximum of the Gaussian function was equated with the period of a sine wave conventionally used to define spatial resolution. This simplification is acceptable (Snyder, 1979) considering that a sine wave can no longer be detected by three neighbouring receptors when the sampling resolution (half-period of the sine wave) corresponds to half the full width at half-maximum of the Gaussian blur induced by the optics. In that situation, the middle receptor sampling the original minimum (no light) will receive an intensity of twice the half-maximum, and its signal is thus indistinguishable from that of the receptors sampling the original maxima.

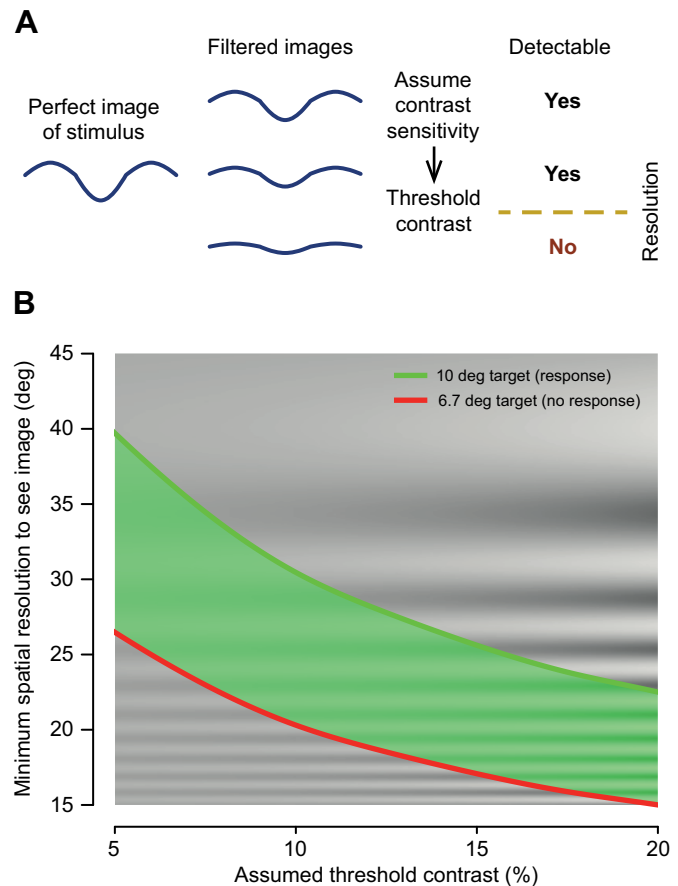


Fig. 9. Spatial resolution of *E. rowelli*. (A) Diagram illustrating the procedure used to estimate spatial resolution. All stimuli in the behavioural experiments consisted of more than one spatial frequency, which precluded the direct deduction of spatial resolution from behavioural responses. Instead, we calculated optical resolution by simulating how the piecewise sine stimuli closest to the behavioural detection threshold appeared to the retina through the under-focused optics of the onychophoran eye. A perfect image of the stimulus pattern (left) was blurred by a Gaussian filter of increasing width, which resulted in a progressive loss of contrast between the two maxima and the minimum in the image (middle). When the remaining contrast reached a threshold value determined by the assumed contrast sensitivity of the animals (right), the optical resolution limit was reached. Because the blur prevents the detection of finer details, we can equate the full width at half maximum of the Gaussian function with the period of a just-resolvable sine wave that is conventionally used to define spatial resolution. For details, see Materials and Methods. (B) Spatial resolution required to detect a piecewise sine stimulus plotted against the range of assumed contrast thresholds. The green range indicates an estimate of the minimal spatial resolution of *E. rowelli*, assuming that the image-forming capacity and contrast sensitivity of the eyes limit the animals' behavioural performance. The upper and lower bounds are based on the results of object taxis towards piecewise sine stimuli (Figs 7 and 8). A sinusoidal background pattern of varying contrast and spatial frequency qualitatively illustrates the image of a sine wave reaching the retina, which the animal would still detect given its contrast sensitivity and spatial resolution.

RESULTS

Eye anatomy and dimensions

Consistent with previous studies on several onychophoran species (Dakin, 1921; Eakin and Westfall, 1965; Mayer, 2006), our light and electron microscopic sections showed that the eye of *E. rowelli* is composed of a multi-layered cornea, an acellular lens, and a light-sensitive rhabdomeric layer surrounded by dark screening pigment, which functionally defines the ocular chamber (Fig. 1). The outermost layers of the cornea are transparent continuations of

the body cuticle and epidermis devoid of dermal protrusions (Fig. 1A,B,D). Having a relatively constant thickness across all eccentricities, the cornea is perfectly flush with the front curvature of the lens. The light-sensitive rhabdomeric layer directly adjoins the rear surface of the lens and fills the whole ocular chamber, leaving no fluid-filled cavities or clear zones. It consists of microvilli that radiate from long processes in different directions and do not appear to be particularly ordered (Fig. 1C,D). The photoreceptor processes penetrate the pigment layer (Fig. 1B) and enter the perikaryal layer, which contains the nuclei of both photoreceptors and pigment cells. Pigment cells are distinguished from photoreceptors by the lack of a rhabdomeric unit and the presence of numerous pigment granules (Mayer, 2006; Eakin and Westfall, 1965).

To determine the shape, exact orientation and dimension of ocular tissues, we reconstructed optically crucial elements of the eyes and the surface of the head of an individual of 32 mm body length (Fig. 2) in 3D based on serial sections. The eyes are located dorsolaterally (Fig. 1A), 1.2 mm apart on either side of the head right behind the antennae (Fig. 2A–E). While the antennae point forward in an active animal as a result of hydrostatic pressure and muscle contraction, they drop during anaesthesia and appear as such in the reconstruction. The pigment layer does not enclose the rhabdomeric layer spherically. Instead, the ocular chamber is flattened centrally, such that its medial boundary runs almost parallel to the body long axis (Fig. 2E,F), and has a pronounced posterior elongation. Because of this asymmetric shape of the eye, the thickness of the rhabdomeric layer varies along different axes through the centre of the lens from about 50 μm in the centre of the eye chamber to 90 μm in the periphery, and reaches up to 100 μm in the posterior elongation for oblique, off-centre axes. As the lens is tilted anteriorly within the eye and the eyes are directed slightly upwards, the shortest axis through the centre of the lens, which is also the axis of symmetry, deviates by about 20 deg upward and 15 deg frontward from a mediolateral orientation (Fig. 2F). The thickness of the lens along this axis (axial thickness) in the two reconstructed eyes is 73 μm , while the diameter at the equator (widest diameter) of the lens is 97 μm .

Isolated fresh lenses are solid and their convex front surface is almost circular (Fig. 3B; average ratio of biggest to smallest equatorial diameter=1.08, s.d.=0.04, $n=10$). In agreement with the shape of the lens in the 3D reconstruction (Fig. 2F), the diameter of fresh lenses tapers considerably towards their rear surface (Fig. 3A). Measurements of the front curvature of fresh lenses conform well to those of sectioned lenses (Table 1), and the equatorial diameter determined from the 3D reconstruction and fresh lenses differs only by a factor of 1.08. However, the axial thickness of fresh lenses is 1.44 times larger than that of reconstructed lenses. This discrepancy might be caused by uneven shrinkage, which occurred during the preparation of fixed samples. Mayer (2006) reports that the onychophoran lens is often shrunken in histological sections, and we noticed that fresh lenses were prone to desiccation if exposed to air.

Measurements of dimensions that change considerably off-axis deviated systematically between physical and virtual sections. The 3D reconstruction facilitated the determination of the shortest axis through the centre of the lens and allowed a careful selection of the sectional plane, whereas this was less precise in physical sections. Except for the values of the cornea, we therefore relied on the 3D reconstruction and fresh lenses for calculating optical parameters. However, all measurements were taken into account to define a range and estimate a lower and upper limit of possible results.

Specimens of *E. rowelli* vary in body length from a few millimetres at birth to several centimetres when adult. To ensure similar eye sizes in all experiments, we tried to select adults that had the same body length. Yet, the limited number of available animals and their changing body length during the time we conducted the study forced us to accept a certain size range. We therefore investigated the relationship between lens diameter (used as a proxy for eye size) and body length in the six animals (27–34 mm in length), for which we had measurements from 10 fresh lenses. As we found no significant linear correlation ($R^2=0.12$, slope=0.34, $P=0.26$), none of our measurements was standardized to body length.

Optics and geometrical eye model

We determined the optical properties of the onychophoran eye in several steps. The even staining of the lens in light microscopic sections (Fig. 1A,D), the lack of an electron density gradient across the lens in transmission electron micrographs (Fig. 1B,C), and the overall flat profile of the lens in DIC images of cryosections (Fig. S1) suggest that the lens might lack graded index optics (for examples of refractive index gradation, see Gagnon et al., 2008; Nilsson, 1990). Hence, we assumed a homogeneous refractive index of the lens in our calculations.

To find the refractive index, we immersed isolated lenses in saline and measured the distance between the lens equator and the back focal plane along the shortest axis through the centre of the lens (Fig. 3). The average of 10 lenses was taken as an approximation of the focal length in saline solution ($f'_{\text{lens}}=275 \mu\text{m}$) and used to get an estimate of the refractive index of the lens (Eqn 1, $n'_{\text{lens}}=1.482$) based on the dimensions of isolated lenses listed in Table 1 and the refractive index of the solution. To obtain a more accurate measure of the focal length and, consequently, the refractive index, we calculated the position of the second principal point of the lens (Eqn 2, $P_{\text{lens}}=-51.3 \mu\text{m}$), from which the true focal distance is specified, using n'_{lens} . As P_{lens} was located in front of the lens back vertex, its absolute value (51.3 μm) was added to f'_{lens} after the distance between the equator and the back vertex of the lens (54.4 μm , Table 1) had been subtracted. With this corrected focal length ($f_{\text{lens}}=272.0 \mu\text{m}$), we revised the value for the refractive index of the lens (Eqn 1), resulting in $n_{\text{lens}}=1.485$.

The cornea is thin (d_{cornea} up to 12.2 μm , Table 1) in comparison to the lens (d_{lens} up to 104.5 μm), perfectly flush with the lens (Fig. 1) and has a similar radius of curvature to the lens front (Table 1). We therefore merged the cornea with the lens for the purpose of our calculations, assuming the same refractive index n_{lens} . For the combined thickness of the cornea and lens ($d=116.7 \mu\text{m}$), a front surface exposed to air ($n_{\text{air}}=1.0003$) and a back surface exposed to the rhabdomeric layer ($n_{\text{rhabdomere}}=1.363$; Nilsson and Howard, 1989), the focal length of the eye was determined as 156.4 μm (Eqn 4, f_{eye}). On the same assumptions, the second principal point of the combined optical system was found to be 25 μm in front of the rear vertex of the lens (Eqn 6, $P_{\text{eye}}=-25.0 \mu\text{m}$). Thus, the back focal distance (focal distance from the rear vertex of the lens) along the shortest axis was 131.3 μm . To account for the variability and uncertainty of our measurements, we also calculated the back focal distance using the most extreme combinations of values in Table 1 and 70.3 μm for the maximal radius of curvature of the cornea R_{cornea} . The latter resulted from adding the maximal corneal thickness d_{cornea} to the maximal radius of curvature of the front surface of the lens $R_{1,\text{lens}}$. That way, we obtained a minimal and maximal estimate for the back focal distance of 117.0 μm and 142.73 μm .

While these are approximate values, which make a number of generalizations, they clearly place the focal point well behind the rhabdomeric layer (thickness 50 μm) in the centre of the eye. This implies that the eye must be under-focused as illustrated in the geometrical model (Fig. 4) based on a section through the 3D reconstruction (Fig. 2F).

Detection of a dark target

Euperipatoides rowelli exhibited a robust taxis to wider targets of both dual bar and piecewise sine stimuli (Figs 6A,B and 7). In the absence of a salient stimulus, paths were undirected, such as in the control (Fig. 6C; no significant deviation from circular uniformity, Watson test: $U_n^2=0.06$, $P>0.10$). However, even for those conditions where animals consistently approached the target, the paths taken were often tortuous (Fig. 6A,B). We determined the headings of the animals at 7.5 cm radial distance from the centre of the arena (Fig. 5C) for a total of 343 trials, between 21 and 27 for each stimulus, including 23 for the control (Fig. 7; Table S2). To assess whether the heading was a suitable prediction of the animal's destination despite the winding tracks, we compared the heading with the point of arrival at the wall. Of the 93 trials for which the animal ultimately approached the target (i.e. reached the wall at the target), the heading was directed towards the target (i.e. was within the angle subtended by the target arc) in 51 cases, including where the target was very narrow. Conversely, of the 227 trials for which the animal did not ultimately approach the target, the heading was directed towards the target in only two cases. This suggests that the headings are a reliable metric to describe the animals' orientation and reflect whether they detect the stimuli.

For both stimulus types, animals were better oriented towards wider stimuli (Fig. 7). This is supported by Kruskal–Wallis tests, which showed significant differences in the distribution of headings between treatments for both the dual bar stimuli ($P<0.01$, $\chi^2=12.2$, d.f.=2) and the piecewise sine stimuli ($P<0.01$, $\chi^2=23.3$, d.f.=10). The headings are clearly concentrated towards the stimulus for the two wider bar targets (25.5 and 51 deg) and for the piecewise sine stimuli with a target width of 10 deg and greater. Consistent with this, Wilcoxon–Mann–Whitney tests indicated a significant difference between the headings of the narrowest dual bar target (12.7 deg) and those of the two wider targets ($P<0.001$, $W=792$), and between the headings of the narrower piecewise sine targets and those of 10 deg and bigger ($P<0.001$, $W=9986$).

Similar results were obtained by a mixed-effects probit regression model, which analysed the success rate, i.e. the proportion of animals heading towards the target quadrant (Figs 7 and 8), taking individual differences into account. The most likely model (Table S1), fitted to the control and to piecewise sine targets of up to 20 deg, included the size of the target as a linear fixed effect. The effect of target size on the probability approaching the target was highly significant ($P<0.001$, $z=3.8$, s.e.m.=0.04). In contrast, the orientation of the target within the experimental room had no significant effect and was thus not considered in the final model.

Spatial resolution

In the experiments on object taxis towards piecewise sine stimuli, we found that *E. rowelli* is probably able to detect a dark target of 10 deg but not 6.7 deg angular width. Using this range as an estimate of the animals' detection threshold and assuming threshold contrasts between 5% and 20% (contrast sensitivities of 20 to 5), our simulation of the under-focused eye of *E. rowelli* predicts a spatial resolution of 15–40 deg (Fig. 9). This is equivalent to the ability to detect a sine wave of the same angular period and suggests that a log

with a diameter of 50 cm becomes resolvable from a distance of 0.7–1.9 m, while adult onychophorans might be able to spot each other from 5–13 cm away and a prey item like a 1 cm cricket from 1–4 cm away.

DISCUSSION

In this study, we found that *E. rowelli* exhibits coarse resolving vision, which is mediated by an under-focused eye design and guides locomotion. To our knowledge, this represents the first report of resolving vision in Onychophora.

Visually guided behaviour with coarse spatial resolution

Behavioural tests for measuring spatial resolution should ideally rely on stimuli with only one spatial frequency. Optomotor responses, such as the constant turning of a walking animal in response to a moving sinusoidal grating, can be used to directly assay spatial resolution by presenting a single spatial frequency. We tried to elicit an optomotor response in onychophorans, but the tortuosity of their walking paths made it impossible to identify an overall turning tendency. Yet, a different set of experiments revealed that the animals were attracted to dark objects like a black bar presented next to a white bar on a grey background. One problem in assessing these responses to determine spatial resolution is that the stimulus contains many spatial frequencies, making it impossible to tell which of these frequencies the animal used for its response. We therefore changed from a dual bar to a piecewise sine stimulus. It consisted of a central sinusoidal dark area surrounded on both sides by sinusoidal bright areas. The dark area and the surrounding bright areas had the same width (i.e. spatial frequency), and the amplitudes of the bright and dark areas were chosen such that the whole stimulus was isoluminant with the grey background displayed at all other angles. Isoluminance is important because it excludes simple phototaxis to a dark object and requires that the animal must resolve the pattern to detect the target. However, even the piecewise sine stimulus contains other spatial frequencies than that of its main sine component, which precludes direct deduction of spatial resolution from the behavioural responses.

Therefore, we used another approach. We calculated optical resolution by simulating how the two stimuli closest to the behavioural detection threshold appeared through the eyes of *E. rowelli*. As the blurring induced by the optics reduces contrast and prevents the detection of finer details, we can infer spatial resolution from optical resolution assuming that the image-forming capacity and contrast sensitivity of the eyes limit the behavioural performance of the animals. Neighbouring photoreceptors in the retina can only resolve a pattern if the contrast in the retinal image exceeds or is equal to a certain threshold. This threshold contrast is the reciprocal of the animals' contrast sensitivity in per cent. Maximal contrast sensitivities among vertebrates have been measured as close to 200 (threshold contrast 0.5%) for humans (De Valois et al., 1974), greater than 100 (threshold contrast 1%) for the cat (Bisti and Maffei, 1974) and in the range of 7 to 31 (threshold contrasts of 14.3% to 3.2%) for birds (Lind et al., 2012). Among insects, maximum contrast sensitivities towards large targets have been estimated to fall in the same range (O'Carroll and Wiederman, 2014): up to 40 (threshold contrast 2.5%) for the blow fly *Calliphora erythrocephala* (Dvorak et al., 1980), and with peaks between 40 and 100 (threshold contrasts between 2.5% and 1.0%) for male hoverflies (O'Carroll and Wiederman, 2014). As no measurements are available for onychophorans, we have to hypothesize, and any computed resolution will thus be associated with an assumed contrast sensitivity. In our calculations, we took a

conservative range of contrast sensitivities from 5 to 20 into account, which yields threshold contrasts from 20% to 5% (Fig. 9). For the same stimulus pattern, a lower assumed contrast threshold (higher contrast sensitivity) allows stronger blurring (a wider Gaussian filter) until the image cannot be resolved anymore. Therefore, the spatial resolution of the eye is most likely worse, meaning that the period of a just-resolvable sine wave is bigger. Conversely, a higher assumed contrast threshold (lower contrast sensitivity) of the animal allows less blurring (a narrower Gaussian filter) for the same stimulus pattern until the image can no longer be resolved. Therefore, the spatial resolution of the eye is most likely better, meaning that the period of a just-resolvable sine wave is smaller. In short, depending on the assumed threshold contrast, we get a different estimate for the spatial resolution and the relationship is inverse.

Apart from the assumed contrast sensitivities, the behavioural estimate of the detection threshold, on which our calculations rely, is also conservative for a variety of reasons. Firstly, some animals turned their heads and bodies and appeared to scan the environment upon release, whereas, in other instances, the animals moved directly to the arena wall, such that the target may have never entered their field of view. Secondly, the animal may detect and perceive the target, but may not always be motivated to approach it. Thirdly, the tortuosity of many of the walking paths introduces further noise and may reduce the clustering of headings towards the target. Thus, the object taxis exhibited in our experiments may not reflect the maximal resolving power of the eye, and it is likely that we underestimate the spatial resolution of the animals.

Interestingly, the proportion of individuals heading towards the target quadrant was highest for piecewise sine stimuli of 20 deg target width (Figs 7 and 8). A decline in the concentration of headings around the centre of the piecewise sine stimuli for wider targets, which were clearly beyond the detection threshold, can be explained in a number of ways. The stimulus pattern of piecewise sine targets wider than 20 deg exceeds 90 deg. Thus, even though the target is still covered by the target quadrant, the whole stimulus is not. A sluggish orientation response can cause headings to be directed towards the bright flanks of the dark target rather than the target itself (cf. 10, 13 and 20 deg target in Fig. 7). If, for wider stimuli, these headings fall outside the target quadrant, they will not be included in the success rate. An alternative and, in fact, antithetic explanation, which seems to fit to the distribution of headings for wider piecewise sine stimuli, is that the bright flanks surrounding the target may become increasingly repellent the bigger they are, driving more animals towards the half of the arena opposite to the target. Moreover, piecewise sine stimuli with targets wider than 20 deg may be less attractive to the onychophorans for reasons specific to their visual system or ecology. The animals may utilize edge detection, i.e. neural filtering to enhance high spatial frequencies that serve as cues to recognize important features of their environment. Finally, the decline in the orientation response to wider targets in the experiments with piecewise sine stimuli could simply be a coincidence. Except for the control, we do not have a measure of variance for the success rate (Fig. 8). However, in view of the tortuous walking paths and the limited number of tested individuals, we expect that the results would vary considerably if we repeated the experiments.

The onychophoran eye is under-focused and produces a blurry image

The possible lack of graded index optics in the eyes of *E. rowelli* is intriguing, as these gradients are abundant in biological lenses,

minimizing spherical aberration and allowing for greater spatial resolution (Land, 2005). There are reports of cases in which differences in the refractive index did not show up clearly in standard light or electron microscopic sections (e.g. Nilsson, 1990). Hence, we also investigated DIC images of cryosections (Fig. S1). We did not notice a consistent distinct slope in the apparent height profile of the lens, which would have indicated a strong refractive index gradient. However, as these sections were stored at -80°C for 2 years before they were imaged, it would be desirable to repeat the investigation with fresh lenses. In addition to qualitative examinations, a quantitative interferometric assessment of fresh lenses (e.g. Nilsson, 1990) is required to provide conclusive evidence of the refractive index profile of the lens.

In any case, the position and organization of the retina alone rule out high acuity vision in *E. rowelli*. The rhabdomeric layer (the site of phototransduction) fills the whole eye chamber, and our calculations for the central part of the eye place the focal plane far beyond the retina (Fig. 4), resulting in an under-focused image. Even if a perfectly focused image fell on the rhabdomeric layer, the unordered network of densely packed, interdigitating microvilli from different photoreceptors (Eakin and Westfall, 1965; Mayer, 2006; cf. Fig. 1C,D) would preclude a better spatial resolution (no well-defined sampling points). Thus, the visual system of *E. rowelli* provides a blurrier image and a lower range of spatial frequencies than feasible for a lens eye of that size. This suggests that *E. rowelli* does not utilize behaviours that require the detection of high spatial frequencies. However, better-focused light through other visual axes may provide greater spatial resolution. The peculiar ellipsoid shape of the eye, the asymmetric lens position (further away from the posterior than the anterior end of the eye) and the tilted orientation of the lens (pointing slightly forward) may improve spatial resolution in the forward direction. To describe the optical capabilities of this eye design in more detail, sophisticated ray-tracing is required.

Visual ecology of onychophorans

The spatial resolution exhibited behaviourally by *E. rowelli* constitutes low-resolution vision (class III in the classification of Nilsson, 2013). While our study has exploited the attraction of this species to dark targets, vision may be used for other tasks and these may drive selection on the resolving power of the visual system. Seeking shelter or identifying specific microhabitats in the foliage by identifying dark areas is commensurate with the object taxis demonstrated in our experiments. Onychophorans are known to avoid bright light (Monge-Nájera et al., 1993; Hering et al., 2012; Beckmann et al., 2015). They dry out easily, and bright parts in their environment may be interpreted as a warning of direct sun exposure. Other possible visual tasks include detection of obstacles and finding a clear path. The spatial resolution we demonstrated in *E. rowelli* is insufficient for spotting or identifying prey and conspecifics beyond a few centimetres from the eye. Onychophorans hunt by spraying an immobilizing adhesive following direct contact with the prey (Read and Hughes, 1987) and will also use this behaviour if threatened. Coarse-resolving vision could possibly aid in aiming the glue spray towards a prey or looming predator at close distance. In addition, social behaviour is reported in *E. rowelli*, including group hunting and feeding, the latter according to a dominance hierarchy (Reinhard and Rowell, 2005). Further experiments involving intraspecific or interspecific interactions in varied light conditions or with blinded specimens could be used to assess the contribution of vision to these behaviours.

Although onychophorans are nocturnal and typically active in dim light (Monge-Nájera et al., 1993), the results presented here were obtained under ample photon availability (Fig. S2). Many animals increase absolute sensitivity at the expense of spatial resolution at low light intensities by optical or neural pooling (Land and Nilsson, 2012). We cannot rule out such a mechanism in *E. rowelli* in general. However, the eye (Fig. 1) revealed no adjustable pupil or other optical structure that would dynamically change both absolute sensitivity and spatial resolution. Photoreceptor responses in onychophoran eyes are slow, suggesting that they lack high temporal resolution, and become even slower with decreasing light intensity (Beckmann et al., 2015). In fact, high temporal resolution is not vitally important to an animal that only moves about 1 cm per second (Monge-Nájera et al., 1993) and hunts primarily using its antennae (Read and Hughes, 1987). The low temporal resolution of its eyes might allow *E. rowelli* to maintain the same coarse spatial resolution down to nocturnal light levels. Overall, the eye design of this species seems to be optimized for enhanced light capture rather than high-acuity vision.

Implications for the evolution of arthropod eyes

Cambrian lobopodians are an assemblage that probably includes the ancestors of modern panarthropods (Liu and Dunlop, 2014) and broadly resemble modern onychophorans. Several fossil forms have cephalic features, which are interpreted as onychophoran-like simple dorsal or lateral eyes (Liu and Dunlop, 2014; Ou et al., 2011; Smith and Caron, 2015), including early Cambrian *Onychodictyon ferox* (Ou et al., 2012), *Miraluolishania haikouensis* (Liu et al., 2004) and *Antennacanthopodia gracilis* (Ou et al., 2011). It is tempting to draw parallels between the eyes of onychophorans and those of ancient lobopodians. However, the fossil evidence is limited and early Cambrian lobopodians were marine, which reduces the refractive power of the cornea and results in rapid attenuation of long-wavelength light within the water column. Nonetheless, given an eye of comparable size, we could anticipate low spatial resolution (class III in the classification of Nilsson, 2013) in early lobopodians, concomitant with the respective repertoire of visual behaviours (e.g. seeking shelter, and shadow or light avoidance). The sophisticated and varied visual organs of arthropods, such as jumping spiders, stomatopods or flying insects (Land and Nilsson, 2012), which can be used for fast interactions with small objects, must have evolved from such a simple progenitor.

Conclusion

Using behavioural experiments based on attraction towards dark objects, we found evidence that the onychophoran *E. rowelli* can truly resolve stimuli that are isoluminant with their background. We calculated spatial resolution to be in the range 15–40 deg, assuming a contrast sensitivity of 5–20. This modest spatial resolution results from an arrangement where the cornea and lens project the image largely behind the retina. Our findings suggest that the eyes play a role in seeking shelter in this species and may be implicated in other behaviours.

Acknowledgements

The authors thank Rita Wallén and Carina Rasmussen for providing anatomical sections, Ola Gustafsson for assistance in the lab, Basil el Jundi for an introduction to Amira, Martin Kohler for carrying out some of the behavioural experiments and the majority of the 3D reconstruction, Julian Reichelt and Lars Hering for contributing the differential interference contrast (DIC) images, and Almut Kelber, Cynthia Tedore, Michael J. Bok, Yakir Gagnon, Eric Hallberg, Tomasz Kozłowski and Sam Powell for valuable advice. We are grateful to Noel Tait, Paul Sunnucks, David Rowell, Ivo de

Sena Oliveira, Franziska Anni Franke, Michael Gerth and Sandra Treffkorn for their assistance with specimen collection.

Competing interests

The authors declare no competing or financial interests.

Author contributions

Conceptualization: M.J.H., D.-E.N.; Methodology: J.S., G.M., M.J.H., D.-E.N.; Software: J.S., M.J.H.; Formal analysis: J.D.K., J.G., J.S., M.J.H.; Investigation: J.D.K., J.G.; Resources: G.M.; Writing - original draft: J.D.K., J.G.; Writing - review & editing: J.D.K., J.S., G.M., M.J.H., D.-E.N.; Visualization: J.D.K., J.G., M.J.H.; Supervision: J.S., M.J.H., D.-E.N.; Project administration: D.-E.N.; Funding acquisition: D.-E.N.

Funding

This project was funded by the Knut och Alice Wallenbergs Stiftelse ('Ultimate Vision' to D.-E.N.).

Supplementary information

Supplementary information available online at <http://jeb.biologists.org/lookup/doi/10.1242/jeb.175802.supplemental>

References

- Bates, D., Mächler, M., Bolker, B. and Walker, S. (2015). Fitting linear mixed-effects models using lme4. *J. Stat. Softw.* **67**, 1–48.
- Beckmann, H., Hering, L., Henze, M. J., Kelber, A., Stevenson, P. A. and Mayer, G. (2015). Spectral sensitivity in Onychophora (velvet worms) revealed by electroretinograms, phototactic behaviour and opsin gene expression. *J. Exp. Biol.* **218**, 915–922.
- Bisti, S. and Maffei, L. (1974). Behavioural contrast sensitivity of the cat in various visual meridians. *J. Physiol.* **241**, 201–210.
- Blaxter, M. and Sunnucks, P. (2011). Velvet worms. *Curr. Biol.* **21**, R238–R240.
- Dakin, W. J. (1921). Memoirs: the eye of *Peripatus*. *J. Cell Sci.* **2**, 163–172.
- De Valois, R. L., Morgan, H. and Snodderly, D. M. (1974). Psychophysical studies of monkey Vision-III. Spatial luminance contrast sensitivity tests of macaque and human observers. *Vision Res.* **14**, 75–81.
- Dewel, R. A. and Dewel, W. C. (1998). The place of tardigrades in arthropod evolution. In *Arthropod Relationships. The Systematics Association Special Volume Series*, vol. **55** (ed. R. A. Fortey and R. H. Thomas), pp. 109–123. Dordrecht, The Netherlands: Springer.
- Dvorak, D., Srinivasan, M. V. and French, A. S. (1980). The contrast sensitivity of fly movement-detecting neurons. *Vision Res.* **20**, 397–407.
- Eakin, R. M. and Westfall, J. A. (1965). Fine structure of the eye of *Peripatus* (Onychophora). *Z. Zellforsch. Mikrosk. Anat.* **68**, 278–300.
- Franke, F. A., Schumann, I., Hering, L. and Mayer, G. (2015). Phylogenetic analysis and expression patterns of Pax genes in the onychophoran *Euperipatoides rowelli* reveal a novel bilaterian Pax subfamily. *Evol. Dev.* **17**, 3–20.
- Gagnon, Y. L., Söderberg, B. and Kröger, R. H. (2008). Effects of the peripheral layers on the optical properties of spherical fish lenses. *JOSA A* **25**, 2468–2475.
- Giribet, G. (2016). Genomics and the animal tree of life: conflicts and future prospects. *Zool. Scr.* **45**, 14–21.
- Greven, H. (2007). Comments on the eyes of tardigrades. *Arthropod Struct. Dev.* **36**, 401–407.
- Gross, V., Treffkorn, S., Mayer, G. (2015). Tardigrada. In *Evolutionary Developmental Biology of Invertebrates 3: Ecdysozoa I: Non-Tetraconata* (ed. A. Wanninger), pp. 35–52. Vienna: Springer.
- Hecht, E. and Zajac, A. (1974). *Optics*. Boston: Addison-Wesley.
- Henze, M. J. and Oakley, T. H. (2015). The dynamic evolutionary history of pancrustacean eyes and opsins. *Integr. Comp. Biol.* **55**, 830–842.
- Hering, L. and Mayer, G. (2014). Analysis of the opsin repertoire in the tardigrade *Hypsibius dujardini* provides insights into the evolution of opsin genes in Panarthropoda. *Genome Biol. Evol.* **6**, 2380–2391.
- Hering, L., Henze, M. J., Kohler, M., Kelber, A., Bleidorn, C., Leschke, M., Nickel, B., Meyer, M., Kircher, M., Sunnucks, P. et al. (2012). Opsins in Onychophora (velvet worms) suggest a single origin and subsequent diversification of visual pigments in arthropods. *Mol. Biol. Evol.* **29**, 3451–3458.
- Kruskal, W. H. and Wallis, W. A. (1952). Use of ranks in one-criterion variance analysis. *J. Am. Stat. Assoc.* **47**, 583–621.
- Land, M. F. (2005). The optical structures of animal eyes. *Curr. Biol.* **15**, R319–R323.
- Land, M. and Nilsson, D.-E. (2012). *Animal Eyes*. New York: Oxford University Press.
- Lind, O., Sunesson, T., Mitkus, M. and Kelber, A. (2012). Luminance-dependence of spatial vision in budgerigars (*Melopsittacus undulatus*) and Bourke's parrots (*Neopsephotus bourkii*). *J. Comp. Physiol. A* **198**, 69–77.
- Liu, J. and Dunlop, J. A. (2014). Cambrian lobopodians: a review of recent progress in our understanding of their morphology and evolution. *Palaeogeogr. Palaeoclimatol. Palaeoecol.* **398**, 4–15.

- Liu, J., Shu, D., Han, J. and Zhang, Z. (2004). A rare lobopod with well-preserved eyes from Chengjiang Lagerstätte and its implications for origin of arthropods. *Chinese Sci. Bull.* **49**, 1063-1071.
- Marshall, J., Carleton, K. L. and Cronin, T. (2015). Colour vision in marine organisms. *Curr. Opin. Neurobiol.* **34**, 86-94.
- Martin, C., Gross, V., Hering, L., Tepper, B., Jahn, H., Oliveira, I. S., Stevenson, P. A. and Mayer, G. (2017). The nervous and visual systems of onychophorans and tardigrades: learning about arthropod evolution from their closest relatives. *J. Comp. Physiol. A* **203**, 565-590.
- Mayer, G. (2006). Structure and development of onychophoran eyes: what is the ancestral visual organ in arthropods? *Arthropod Struct. Dev.* **35**, 231-245.
- Mayer, G., Franke, F. A., Treffkorn, S., Gross, V. and Oliveira, I. S. (2015). Onychophora. In *Evolutionary Developmental Biology of Invertebrates 3: Ecdysozoa I: Non-Tetraconata* (ed. A. Wanninger), pp. 53-98. Vienna: Springer.
- Monge-Nájera, J., Barrientos, Z. and Aguilar, F. (1993). Behavior of *Epiperipatus biolleyi* (Onychophora: Peripatidae) under laboratory conditions. *Rev. Biol. Trop.* **41**, 689-696.
- Nilsson, D.-E. (1990). Three unexpected cases of refracting superposition eyes in crustaceans. *J. Comp. Physiol. A* **167**, 71-78.
- Nilsson, D.-E. (1994). Eyes as optical alarm systems in fan worms and ark clams. *Philos. Trans. R. Soc. B Biol. Sci.* **346**, 195-212.
- Nilsson, D.-E. (2013). Eye evolution and its functional basis. *Vis. Neurosci.* **30**, 5-20.
- Nilsson, D.-E. and Howard, J. (1989). Intensity and polarization of the eyeshine in butterflies. *J. Comp. Physiol. A* **161**, 51-56.
- Nilsson, D.-E., Gislén, L., Coates, M. M., Skogh, C. and Garm, A. (2005). Advanced optics in a jellyfish eye. *Nature* **435**, 201-205.
- O'Carroll, D. C. and Wiederman, S. D. (2014). Contrast sensitivity and the detection of moving patterns and features. *Philos. Trans. R. Soc. Lond. B. Biol. Sci.* **369**, 20130043.
- Oliveira, I. d. S., Read, V. M. S. J. and Mayer, G. (2012). A world checklist of Onychophora (velvet worms), with notes on nomenclature and status of names. *ZooKeys* **211**, 1-70.
- Ou, Q., Liu, J., Shu, D., Han, J., Zhang, Z., Wan, X. and Lei, Q. (2011). A Rare onychophoran-like lobopodian from the Lower Cambrian Chengjiang Lagerstätte, Southwestern China, and its phylogenetic implications. *J. Paleontol.* **85**, 587-594.
- Ou, Q., Shu, D. and Mayer, G. (2012). Cambrian lobopodians and extant onychophorans provide new insights into early cephalization in Panarthropoda. *Nat. Commun.* **3**, 1261.
- Petie, R., Hall, M. R., Hyldahl, M. and Garm, A. (2016). Visual orientation by the crown-of-thorns starfish (*Acanthaster planci*). *Coral Reefs* **35**, 1139-1150.
- Read, V. M. S. J. and Hughes, R. N. (1987). Feeding behaviour and prey choice in *Macropripatus torquatus* (Onychophora). *Proc. R. Soc. B Biol. Sci.* **230**, 483-506.
- Reid, A. L. (1996). Review of the Peripatopsidae (Onychophora) in Australia, with comments on peripatopsid relationships. *Invertebr. Taxon.* **10**, 663-936.
- Reinhard, J. and Rowell, D. M. (2005). Social behaviour in an Australian velvet worm, *Euperipatoides rowelli* (Onychophora: Peripatopsidae). *J. Zool.* **267**, 1-7.
- Robson, E. A., Lockwood, A. P. M. and Ralph, R. (1966). Composition of the blood in Onychophora. *Nature* **209**, 533.
- Schmidt-Rhaesa, A. (2001). Tardigrades - are they really miniaturized dwarfs? *Zool. Anz.* **240**, 549-555.
- Smith, M. R. and Caron, J.-B. (2015). *Hallucigenia's* head and the pharyngeal armature of early ecdysozoans. *Nature* **523**, 75-78.
- Smith, M. R. and Ortega-Hernández, J. (2014). *Hallucigenia's* onychophoran-like claws and the case for Tactopoda. *Nature* **514**, 363-366.
- Snyder, A. W. (1979). The physics of vision in compound eyes. In *Handbook of Sensory Physiology*, Vol. VII/6A (ed. H. Autrum), pp. 225-313. Berlin: Springer-Verlag.
- Strausfeld, N. J., Strausfeld, C. M., Stowe, S., Rowell, D. and Loesel, R. (2006). The organization and evolutionary implications of neuropils and their neurons in the brain of the onychophoran *Euperipatoides rowelli*. *Arthropod Struct. Dev.* **35**, 169-196.
- Zhang, Z. Q. (2011). Animal Biodiversity: An Outline of Higher-Level Classification and Survey of Taxonomic Richness. Auckland: Magnolia Press.
- Zhang, Z. Q. (2013). Animal biodiversity: an update of classification and diversity in 2013. *Zootaxa* **3703**, 5-11.

Table of contents

Figure S1: Differential interference contrast (DIC) images of lenses	1
Figure S2: Choice of illumination for behavioural setup from three artificial light sources	2
Figure S3: Diagnostic plot for the fit of the probit regression model	3
Table S1: Mixed effects probit regression models for analysing success rates	3
Table S2: Outcome of behavioural trials assessing object taxis	link on page 4
Movie 1: A 3D reconstruction of the head and eyes of <i>Euperipatoides rowelli</i>	link on page 4
Reference	4

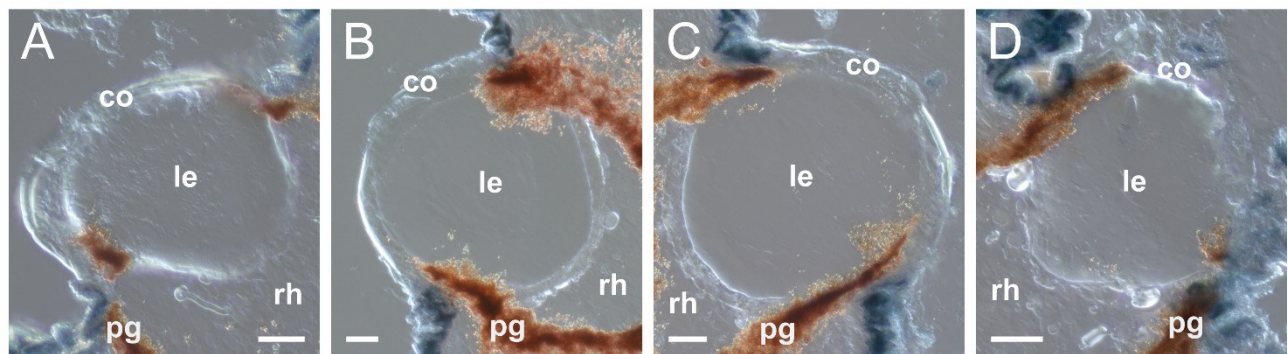


Fig. S1. Differential interference contrast (DIC) images of lenses. (A-D) Cryosections through the dioptic apparatus of the left and right eye of an adult specimen of *Euperipatoides rowelli*. There are no major slopes in the apparent height profile of the lens, which would indicate a strong refractive index gradient. Instead, the overall profile of the lens is flat. Slight differences are likely caused by processing artefacts, given that they are not consistent across sections. The same applies to the apparent ridge in the rhabdomeric layer bordering the lens in B and C. It probably results from thicker tissue that accumulated at the edge of the comparatively hard lens, when the eye was cut from the inside towards the cornea. Scale bars are 20 μm ; co, cornea; le, lens; pg, pigment layer; rh, rhabdomeric layer.

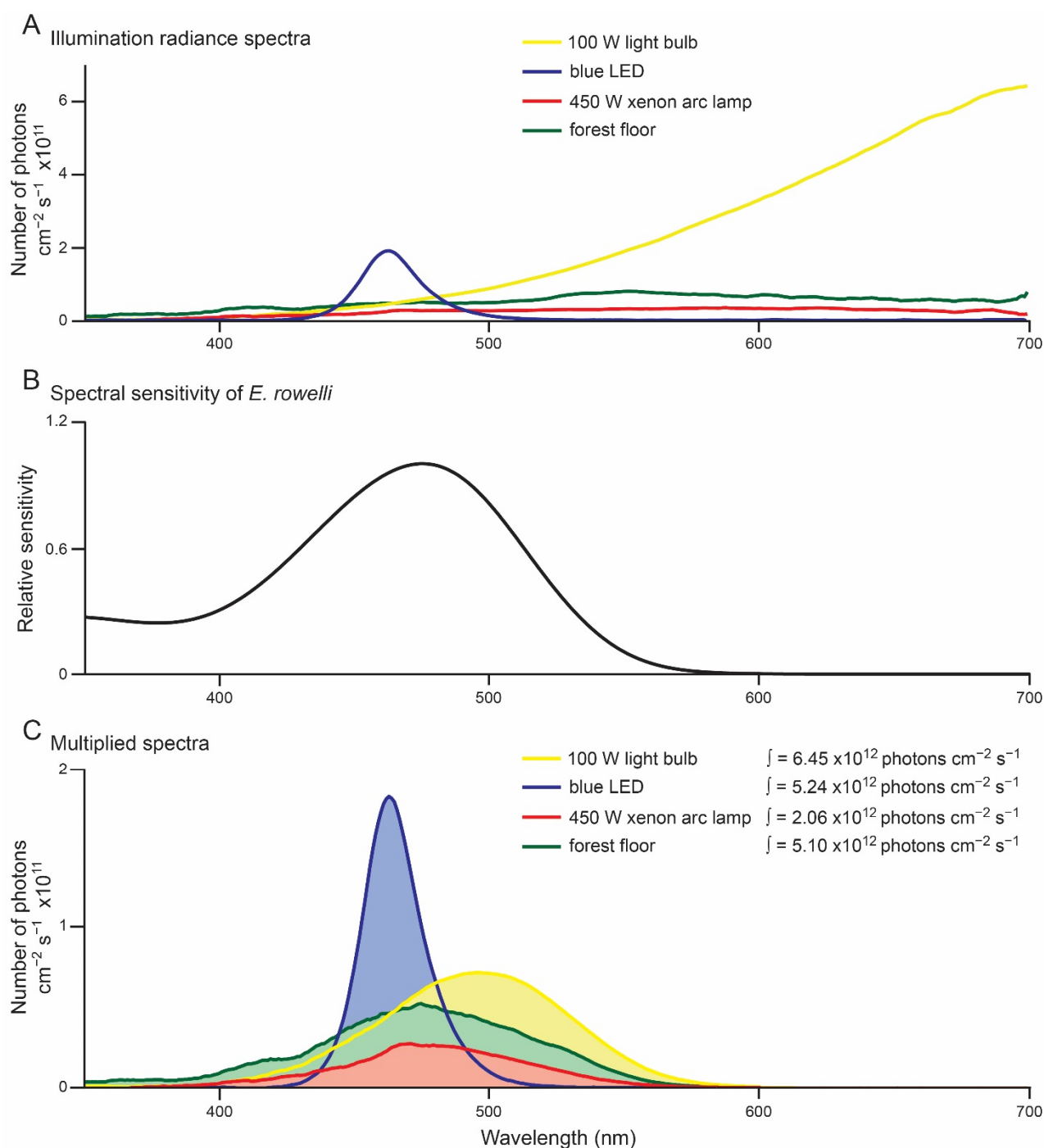


Fig. S2. Choice of illumination for the behavioural setup from three artificial light sources: a light bulb (100 W, Osram Sylvania, Danvers, MA, USA), a blue LED (LXHL-MB1D, Luxeon Star, Brantford, Canada), and a xenon arc lamp (450 W, Malipiero AV Technik, Zurich, Switzerland) combined with a UV-VIS-transmitting light guide. (A) The radiance spectrum of the light reaching the centre of the arena floor through a milk glass diffuser was measured using a calibrated spectroradiometer (RSP900-R; International Light, Peabody, MA, USA) directed towards a white standard (WS-2, TOP Sensor Systems, Eerbeek, the Netherlands) on the arena floor. As a comparison from nature, we recorded the radiance spectrum reflected from the white standard at ground level in a copse during overcast weather in southern Sweden (55° 42' 49.285"N, 13° 12' 29.589"E, October 2014, 10:00-11:00 h local time). All spectra were multiplied by the spectral sensitivity of *Euperipatoides rowelli* (B; Beckmann et al., 2015) and the resulting curves (C) were integrated from 350 to 700 nm to estimate the relative amount of light perceivable by the onychophorans in each case.

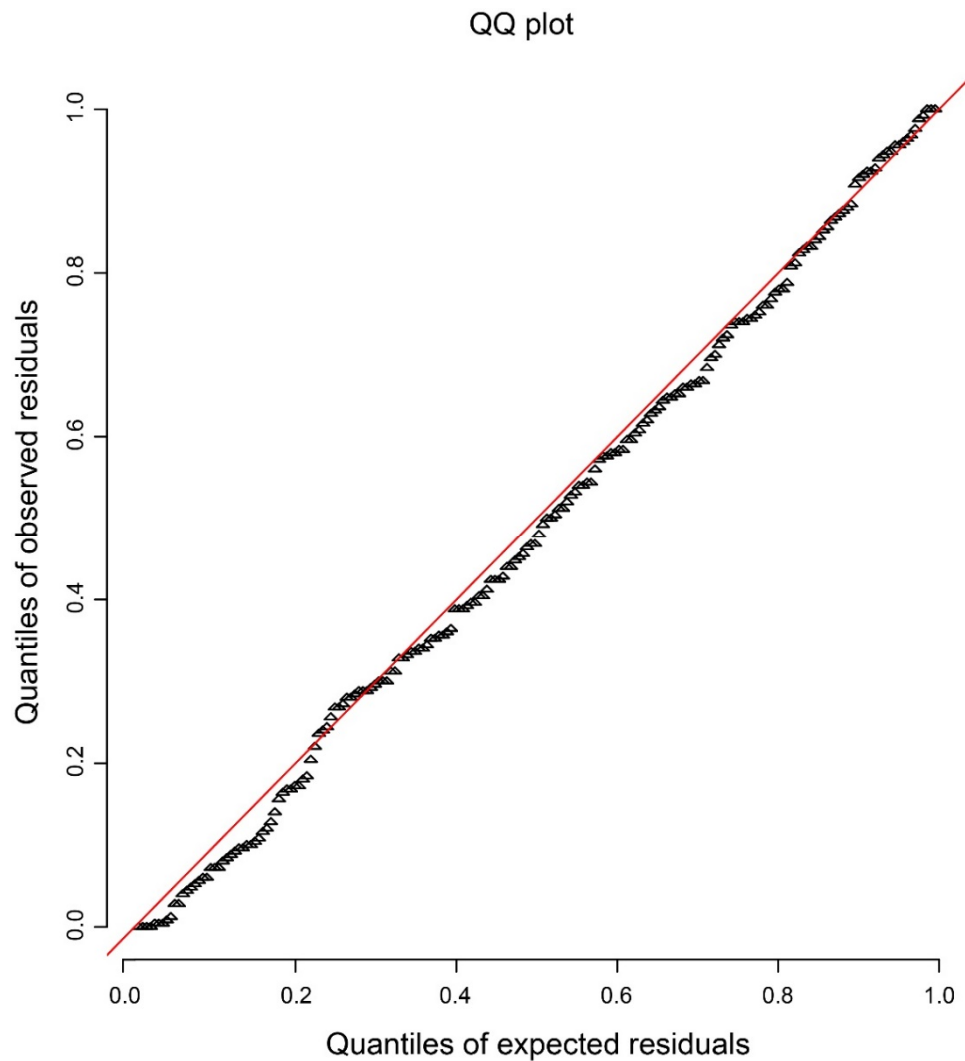


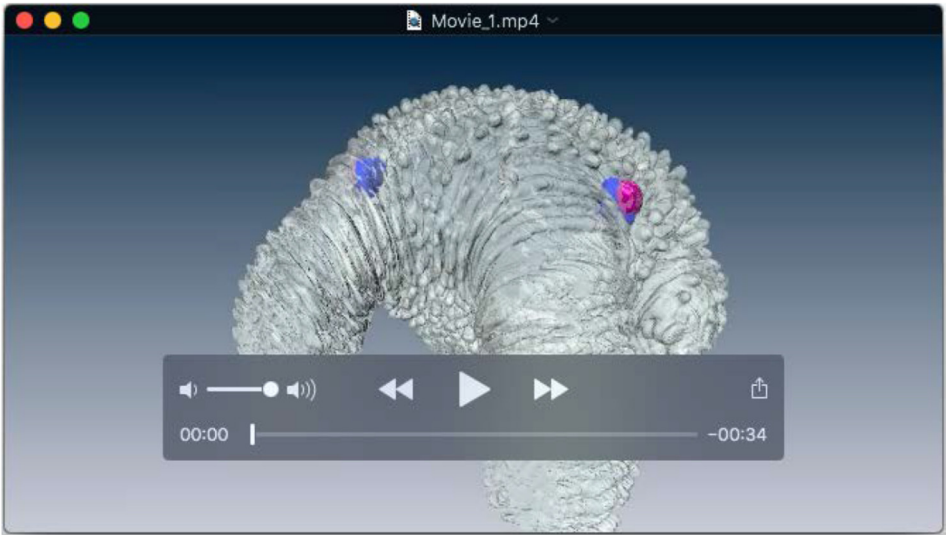
Fig. S3. Diagnostic plot for the fit of the probit regression model. The observed residuals were derived from an empirical cumulative density function for data simulated at each observation based on the model fit. The quantiles of these residuals, scaled from 0 to 1, are plotted against the quantiles of an expected uniform distribution. For a perfect model, all points should adhere to the red line.

Table S1. Tested mixed effects probit regression models for analysing success rates. In all cases, random intercepts were included for individual effects. M1 was selected as the most likely model from the list below based on the lowest value of the Akaike information criterion.

model	fixed effects	degrees of freedom	Akaike information criterion (AIC)
M1	stimulus width	3	236.0573
M2	stimulus width + orientation	6	241.6625
M3	stimulus width x orientation	9	246.9222 (did not converge)
null	no fixed effect	2	256.2287

Table S2: Outcome of behavioural trials assessing object taxis

Trial	Individual	Stimulus type	Target arc angle (deg)	Orientation of setup	Date of trial (YYYYMMDD)	Heading (deg)	Orientation success
1	11	control	0	East	20120829	297.43	FALSE
2	12	control	0	North	20120828	286.26	FALSE
3	13	control	0	North	20120830	89.04	FALSE
4	16	control	0	North	20120829	12.76	TRUE
5	17	control	0	East	20120829	208.15	FALSE
6	18	control	0	West	20120829	335.88	TRUE
7	19	control	0	East	20120829	308.39	FALSE
8	20	control	0	South	20120829	350.65	TRUE
9	21	control	0	North	20120829	198.02	FALSE



Movie 1: A 3D reconstruction of the head and eyes of an adult specimen of *Euperipatoides rowelli*. The cornea is coloured in pink and the surface of the head (grey) is shown partially transparent to expose the pigment layer (blue), which functionally defines the ocular chamber.

Reference

Beckmann, H., Hering, L., Henze, M. J., Kelber, A., Stevenson, P. A. and Mayer, G. (2015). Spectral sensitivity in Onychophora (velvet worms) revealed by electroretinograms, phototactic behaviour and opsin gene expression. *J. Exp. Biol.* 218, 915-922.